Study of the 2D laminar flapping wing case using the Spectral Difference method

by

Junfeng Wang, Chunlei Liang

Department of Mechanical and Aerospace Engineering
George Washington University
Washington DC, 20052
Phone: (202) 994-7073
chliang@gwu.edu

1st International Workshop on High-Order CFD Methods

1   Code description

We further developed a 2D spectral difference (SD) method code published in [1] and [2] to handle moving and deformable grids. The code is written using the spectral difference method where the solution points and flux points are arranged in a staggered fashion. We typically conduct computations using either 3rd-, 4th-, 5th-, or 6th-order SD method. The flow field within each cell is reconstructed with a smooth representation using a tensor-product form. The discontinuity across cell interfaces is handled using a Rusanov flux (Local Lax Friedrichs method). We also implemented a p-multigrid scheme for this solver. For this abstract, all results are obtained using a single-level grid with the 5rd-order SD emthod.

The mesh deformation and translation are controlled using a blended function as suggested in [3] and adopted in [4]. The current form of implementation for moving and deformable grid has similarity with the one reported in [5].

Consider unsteady conservation laws only in 2D conservative form

$$\frac{\partial \mathbf{Q}}{\partial t} + \frac{\partial F}{\partial x} + \frac{\partial G}{\partial y} = \frac{\partial \mathbf{Q}}{\partial t} + \nabla \mathbf{F}_{inv}(\mathbf{Q}) - \nabla \mathbf{F}_v(\mathbf{Q}, \nabla \mathbf{Q}) = 0 \tag{1}$$

where Q is the vector of conserved variables; F and G are the total fluxes including both inviscid and viscous flux vectors.

Consider only compressible Navier-Stokes equations, the conservative variables $\mathbf{Q}$ and Cartesian components $f_{inv}(\mathbf{Q})$ and $g_{inv}(\mathbf{Q})$ of the inviscid flux vector $\mathbf{F}_{inv}(\mathbf{Q})$ are given by

$$\mathbf{Q} = \left\{ \begin{array}{c} \rho \\ \rho u \\ \rho v \\ E \end{array} \right\}, \quad f_{inv}(\mathbf{Q}) = \left\{ \begin{array}{c} \rho u \\ \rho u^2 + p \\ \rho uv \\ u(E + p) \end{array} \right\}, \quad g_{inv}(\mathbf{Q}) = \left\{ \begin{array}{c} \rho v \\ \rho uv \\ \rho v^2 + p \\ v(E + p) \end{array} \right\} \tag{2}$$

where ρ is the density, u and v are the velocity components in x and y directions, p stands for pressure and E is the total energy. The pressure is related to the total energy by

$$E = \frac{p}{\gamma - 1} + \frac{1}{2}\rho(u^2 + v^2) \tag{3}$$

with a constant ratio of specific heat γ set as 1.4 for air.

The Cartesian components $f_v(\mathbf{Q}, \nabla\mathbf{Q})$ and $g_v(\mathbf{Q}, \nabla\mathbf{Q})$ of viscous flux vector $\mathbf{F}_v(\mathbf{Q}, \nabla\mathbf{Q})$ are given by

$$f_v = \mu \left\{ \begin{array}{c} 0 \\ 2u_x + \lambda(u_x + v_y) \\ v_x + u_y \\ u \cdot f_{v[2]} + v \cdot f_{v[3]} + \frac{C_p}{P_r}T_x \end{array} \right\}, g_v = \mu \left\{ \begin{array}{c} 0 \\ v_x + u_y \\ 2v_y + \lambda(u_x + v_y) \\ u \cdot g_{v[2]} + v \cdot g_{v[3]} + \frac{C_p}{P_r}T_y \end{array} \right\}$$

where μ is the dynamic viscosity, C_p is the specific heat and P_r stands for Prandtl number. T is temperature which can be derived from the perfect gas assumption. λ is set to $-2/3$ according to the Stokes hypothesis.

To achieve an efficient implementation, all quadrilateral elements in the moving and deformable physical domain (x, y, t) are transformed into a square element $(0 \le \xi \le 1, 0 \le \eta \le 1, \tau = t)$ as shown in figure 1. The governing equations in the physical domain are then transferred into the computational domain, and the transformed equations are written as:

$$\frac{\partial \tilde{\mathbf{Q}}}{\partial \tau} + \frac{\partial \tilde{\mathbf{F}}}{\partial \xi} + \frac{\partial \tilde{\mathbf{G}}}{\partial \eta} = 0 \tag{4}$$

where $\begin{bmatrix} \tilde{\mathbf{F}} & \tilde{\mathbf{G}} & \tilde{\mathbf{Q}} \end{bmatrix}^T = |\mathcal{J}|\mathcal{J}^{-1}\begin{bmatrix} \mathbf{F} & \mathbf{G} & \mathbf{Q} \end{bmatrix}^T$. The Jacobian matrix is given by

$$\mathcal{J} = \frac{\partial(x, y, t)}{\partial(\xi, \eta, \tau)} = \begin{bmatrix} x_\xi & x_\eta & x_\tau \\ y_\xi & y_\eta & y_\tau \\ 0 & 0 & 1 \end{bmatrix}, \tag{5}$$

where $t_\xi = 0$, $t_\eta = 0$, and $t = \tau$.

In the standard element, two sets of points are defined, namely the solution points and the flux points, as illustrated in figure 1 (b) for a computational cell. A bilinear mapping is employed to map individual physical cells shown in Fig. 1 (a) to this standard computational cell.

In order to construct a degree $(N - 1)$ polynomial in each coordinate direction, N solution points are required. The solution points in 1D are chosen to be the Chebyshev-Gauss points. The flux points $X_{s+1/2}$ are selected as the Legendre-Gauss-quadrature points plus the two end points, 0 and 1, as suggested by following [6] and [7].

Using the solutions at N solution points, a degree $(N-1)$ polynomial can be built using the following Lagrange basis of $h_i(X)$. Similarly, using the fluxes at $(N + 1)$ flux points, a degree N polynomial can be built for the flux using a similar Lagrange basis of $l_{i+1/2}(X)$.

The reconstructed solution for the conserved variables in the standard element is just the tensor products of the two one-dimensional polynomials. The reconstructed flux polynomials are
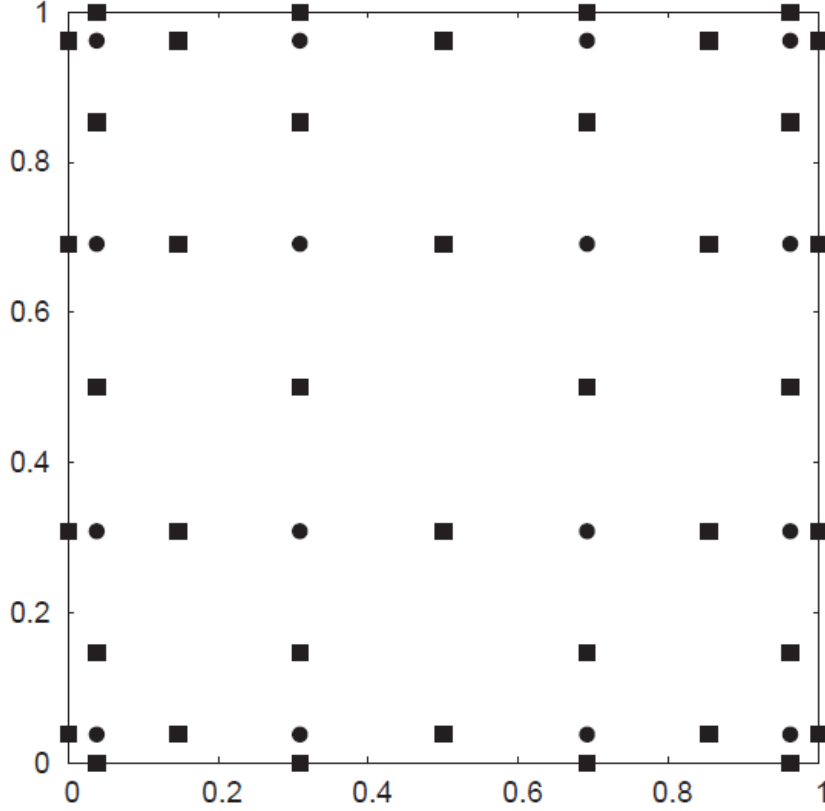
Figure 1: Physical cells and computational cell.

treated in ξ, and η directions as 1D element-wise continuous functions, but discontinuous across cell interfaces. For the inviscid flux, a Riemann solver is employed to compute a common flux at interfaces to ensure conservation and stability. For the viscous flux, an averaging procedure is used.

For dynamic grids considered here, we reformulate the Rusanov solver for the ξ direction as

$$\tilde{F}^{inv} = \frac{1}{2}\left\{ \tilde{F}_L^{inv} + \tilde{F}_R^{inv} - (|\overline{V}_n| + \overline{c}) \cdot (Q_R - Q_L) \cdot |\mathcal{J}\nabla\xi| \cdot s \right\}, \tag{6}$$

where s is the sign of $\mathbf{n} \cdot \nabla\xi$, V_n is the fluid velocity normal to edge interface and c is the speed of sound. For the η direction, it is formulated similarly.

In addition, we must consider geometric conservation law for deforming grid cells:

$$\frac{\partial |\mathcal{J}|}{\partial \tau} + \frac{\partial(|\mathcal{J}|\xi_t)}{\partial \xi} + \frac{\partial(|\mathcal{J}|\eta_t)}{\partial \eta} = 0 \tag{7}$$

The final compact form after taking into account of the geometric conservation law is given by

$$\frac{\partial Q}{\partial \tau} = \frac{1}{|\mathcal{J}|}\left\{ Q\left[\frac{\partial(|\mathcal{J}|\xi_t)}{\partial \xi} + \frac{\partial(|\mathcal{J}|\eta_t)}{\partial \eta}\right] - \left[\frac{\partial \tilde{F}}{\partial \xi} + \frac{\partial \tilde{G}}{\partial \eta}\right] \right\}. \tag{8}$$

Equation 8 has a compact form on the computational domain. It offers great ease in handling moving and deformable physical domain as well as parallel computation.

1.1 Time marching scheme

All preliminary computations in this abrstract utilize a fourth-order accurate, strong-stability-preserving five-stage Runge-Kutta scheme [8].

2 Case summary

The case number C3.4 is investigated in this report. We ran the simulations on a serial computer. The explicit five-stage Runge-Kutta scheme is used with the fifth-order SD method for temporal and spatial discretizations respectively. The time step size is set to 5×10^{-5}.

3 Meshes

We employ an unstructured grid with all quadrilateral cells as shown in Fig. 2 (a). The mesh has 8240 cells in all. It empolys 60 cells around the periphery of the cylinder and 60 cells along either top or bottom half surface of the airfoil. The inflow boundary is 50 diameter away from
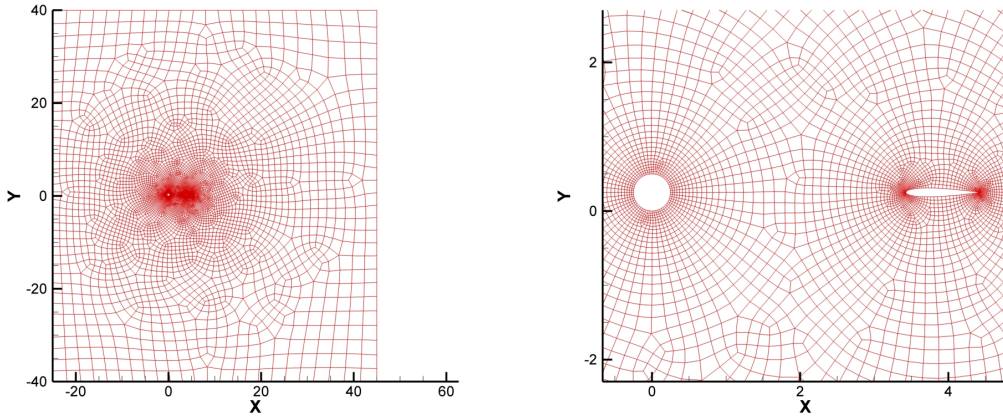
(a) Global view of the computational mesh. (b) Close view of the computational mesh.

Figure 2: Mesh

the cylinder center. The top and bottom boundaries are 80 diameters away from the cylinder center, where the inviscid wall boundary condition is adopted. The outflow flow boundary locates at 90 cylinder diameters downstream the cylinder center.

A close view of the mesh is shown in Fig. 2 (b). The mesh near the cylinder and airfoil is much finer than that in other regions.

The curved surfaces of the cylinder and the airfoil are handled using a cubic spline fitting. Subsequently, the elements adjacent to the surfaces are mapped to a standard square element with 20 nodal points via a cubic-order mapping.

4 Results

The lift and drag forces of cylinder are normalized using $\rho u_\infty^2 D$ where D is the diameter of the cylinder. The lift and drag forces of airfoil are normalized using $\rho u_\infty^2 C$ where C is the chord of the the airfoil. The time coordinate is not normalized and the upstream velocity $u_\infty = 1.0$.

4.1 case s=3.76

A series of contour plots of the vorticity field at four selected phases are shown in Fig. 3.

Drag and lift coefficients for the cylinder are shown in Fig. 4. Drag and lift coefficients for the airfoil are shown in Fig. 5. All these simulations run after a steady state have been established which is at time t=10.64.
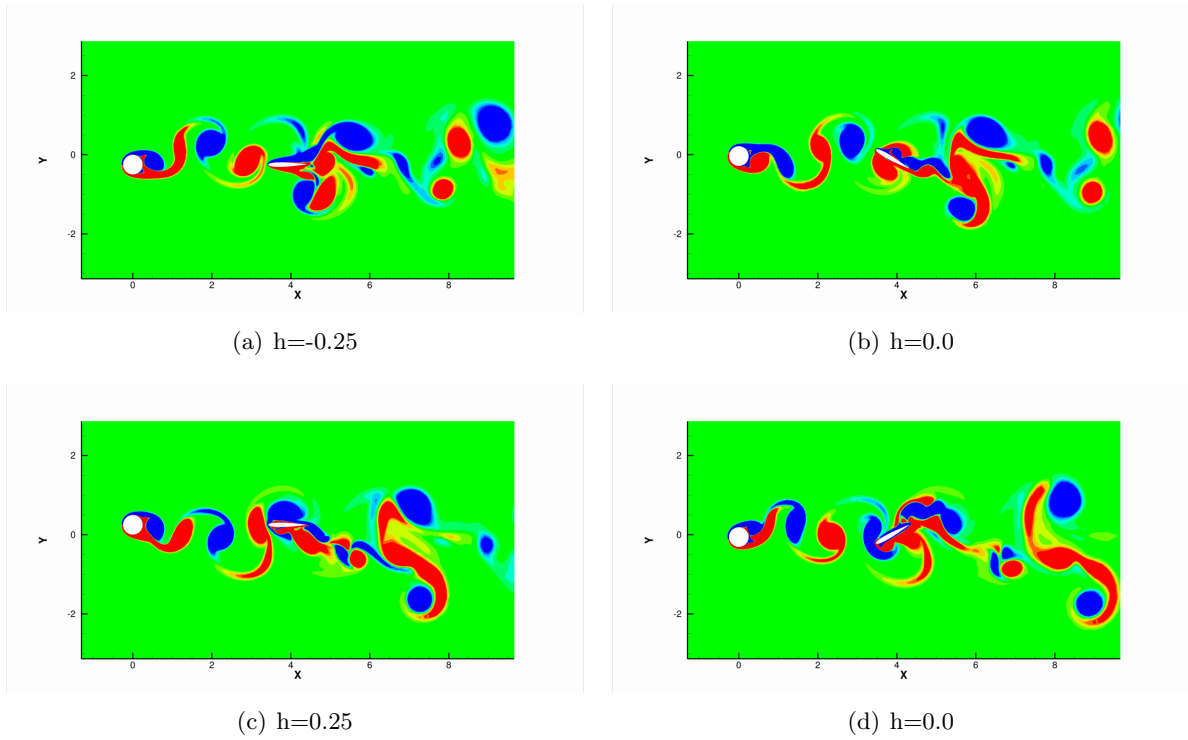
(a) h=-0.25

(b) h=0.0

(c) h=0.25

(d) h=0.0

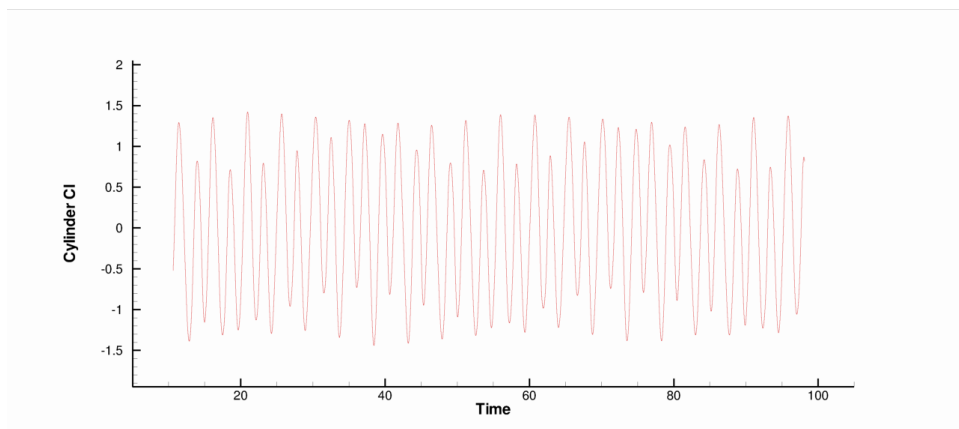Figure 3: Case s=3.76 voticity contours in one stroke period
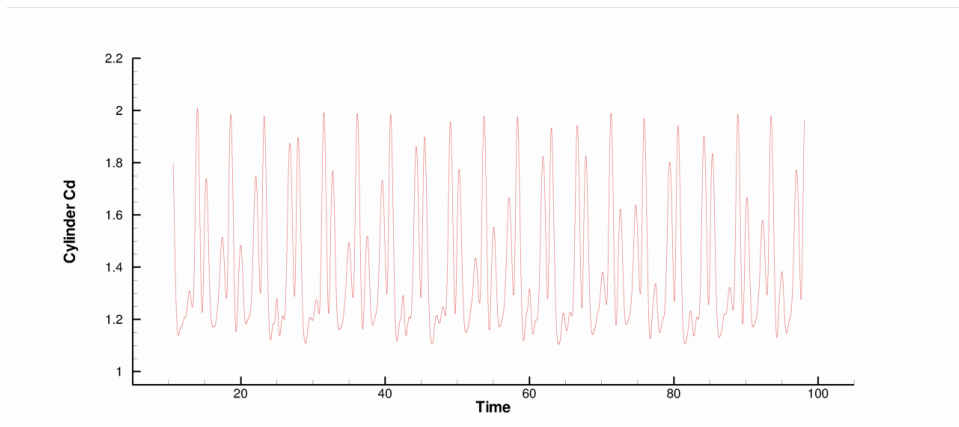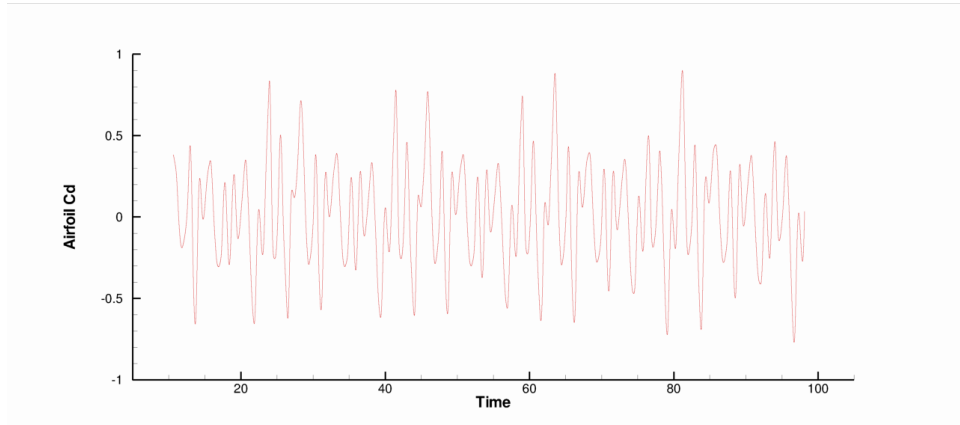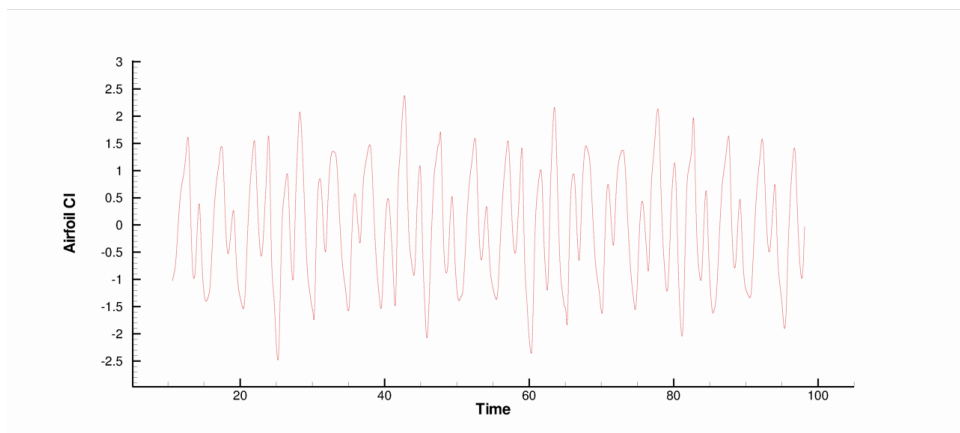

(a) Cylinder Cd

(b) Cylinder Cl

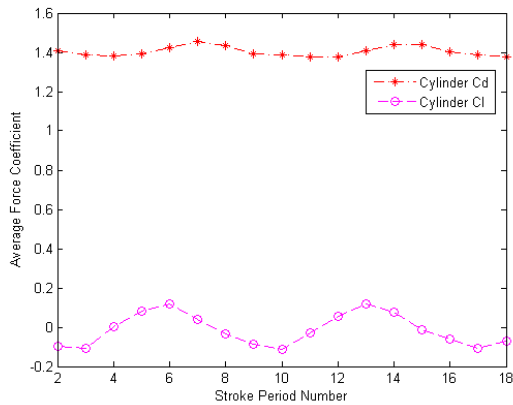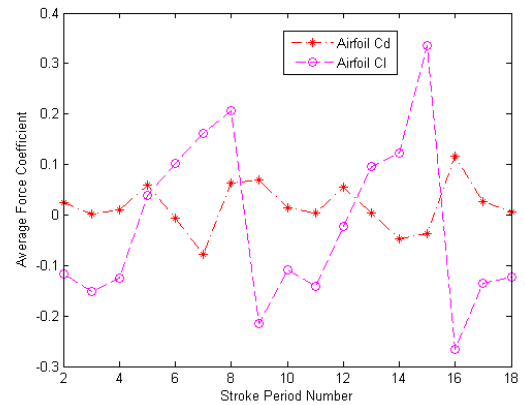Figure 4: Case s=3.76 cylinder drag and lift coefficients

5

(a) Airfoil Cd

(b) Airfoil Cl

Figure 5: Case s=3.76 airfoil drag and lift coefficients

(a) Cylinder average force coefficients

(b) Airfoil average force coefficients
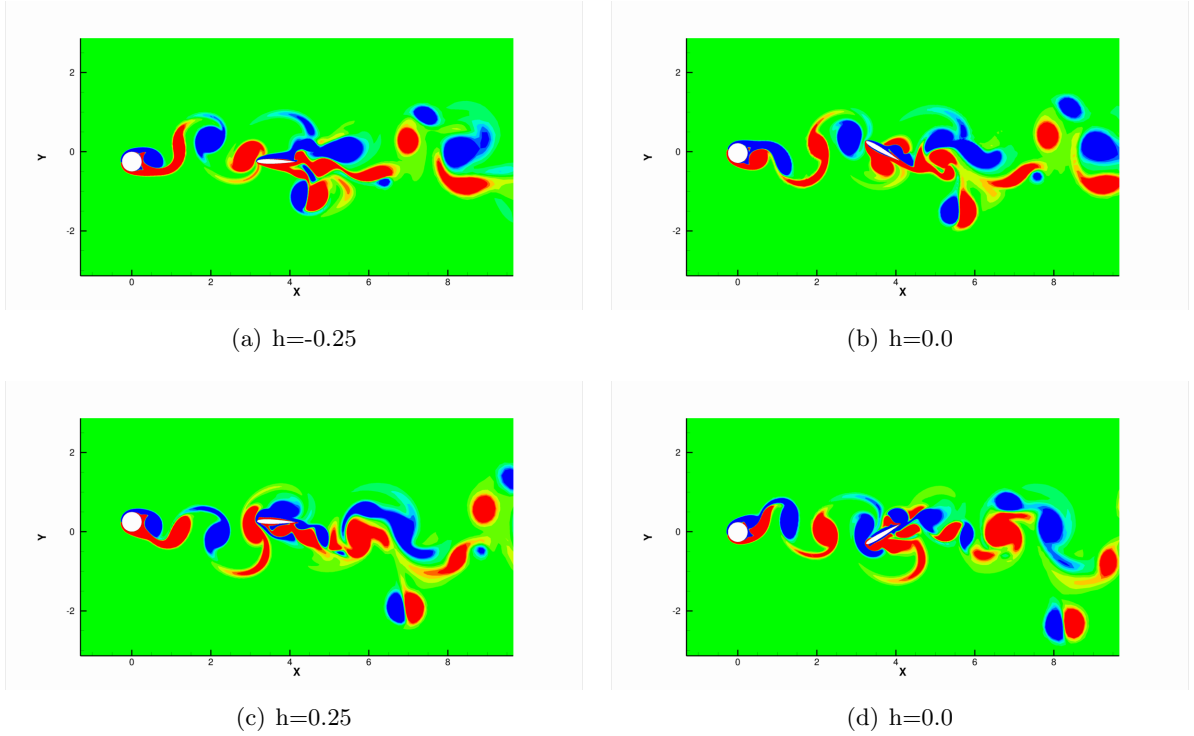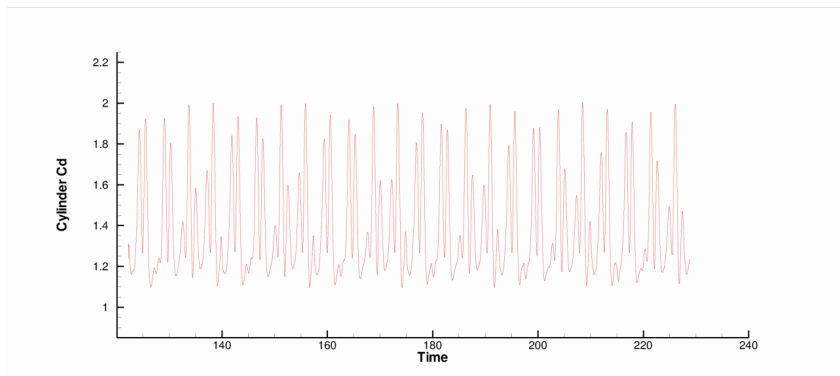
Figure 6: Case s=3.76 average force coefficients

(a) h=-0.25   (b) h=0.0

(c) h=0.25   (d) h=0.0

Figure 7: Case s=3.5 vorticity contours in one stroke period

The average force coefficients during each stroke period are given in Fig. 6. The average cylinder drag and lift coefficients within one stroke are not constants. The cylinder average drag coefficient slightly changes near 1.4 and lift coefficient oscillates near 0.0 with time.
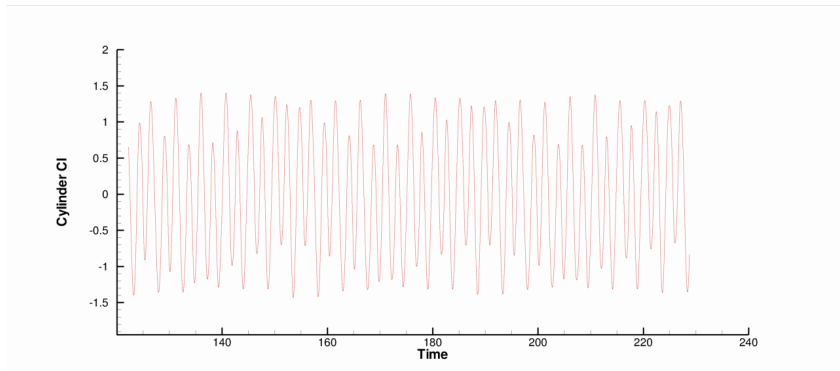
4.2   case s=3.5

A series of contour plots of the vorticity field at four selected phases are shown in Fig. 7. In this case, flow features indicated by vorticity contour between the cylinder and airfoil resembles that of the case s=3.76. However, flow features vary a lot behind the airfoil due to the distance change.

Drag and lift coefficients for the cylinder are shown in Fig. 8. Drag and lift coefficients for the airfoil are shown in Fig. 9. All these simulations run after a steady state have been established which is at time t=122.24.

The average force coefficients during each stroke period are given in Fig. 10.

4.3   case s=3.76 with double frequency

A series of contour plots of the vorticity field at four selected phases are shown in Fig. 11. In this case, flow features indicated by vorticity contour between the cylinder and airfoil are totally different from that of the case s=3.76.

Drag and lift coefficients for the cylinder are shown in Fig. 12. Drag and lift coefficients for the airfoil are shown in Fig. 13. All these simulations run after a steady state have been established which is at time t=60.0.

The average force coefficients during each stroke period are given in Fig. 14. It is emphasized here that, the airfoil average Cl is positive and Cd is negative, which means that the airfoil tends to go forward and lift up in this case.
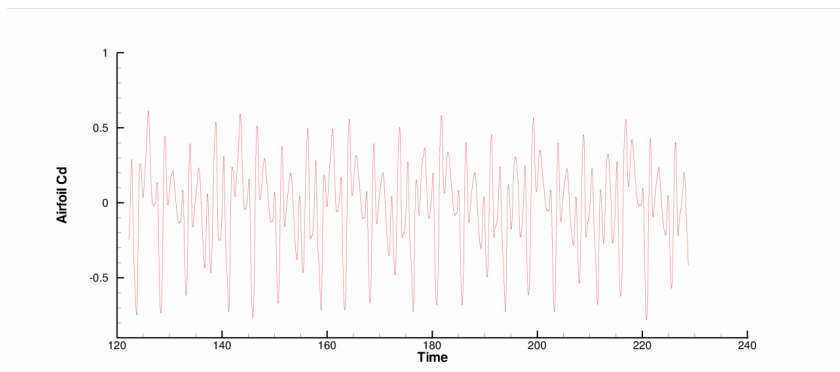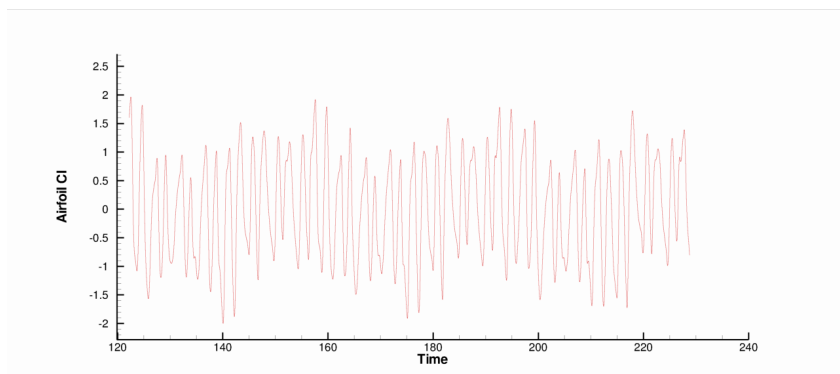
7

(a) Cylinder Cd

(b) Cylinder Cl

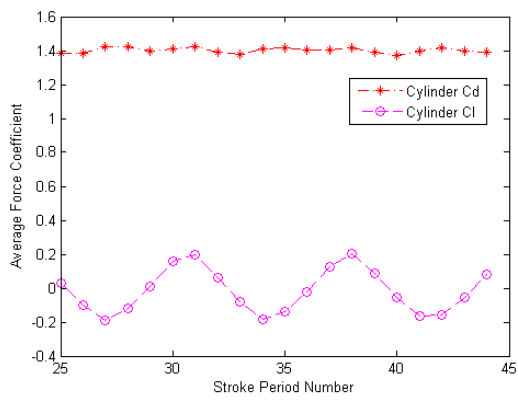Figure 8: Case s=3.5 cylinder drag and lift coefficients
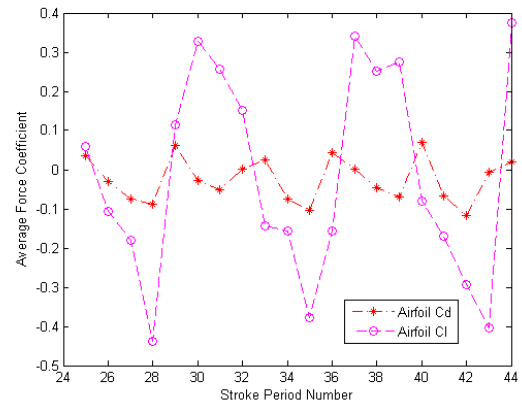

(a) Airfoil Cd

(b) Airfoil Cl

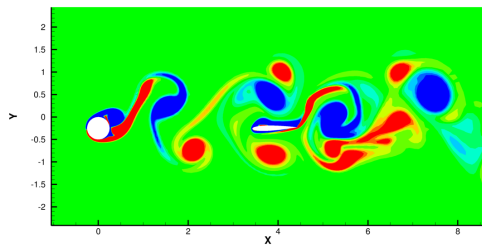Figure 9: Case s=3.5 airfoil drag and lift coefficients
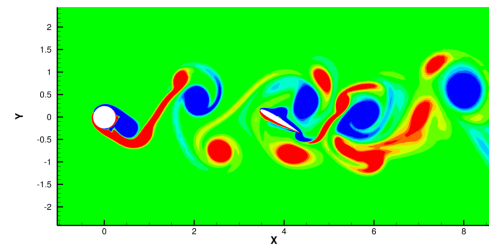
8

(a) Cylinder average force coefficients
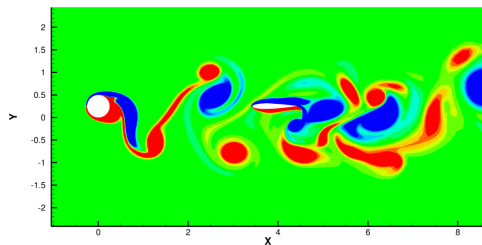
(b) Airfoil average force coefficients

Figure 10: Case s=3.5 average force coefficients

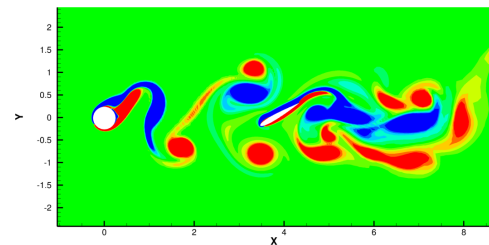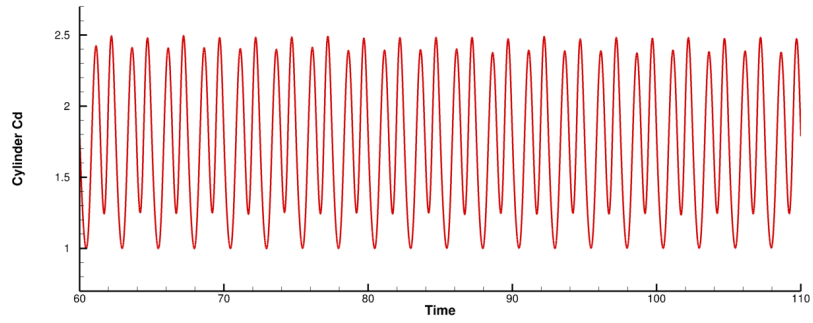

(a) h=-0.25

(b) h=0.0

(c) h=0.25
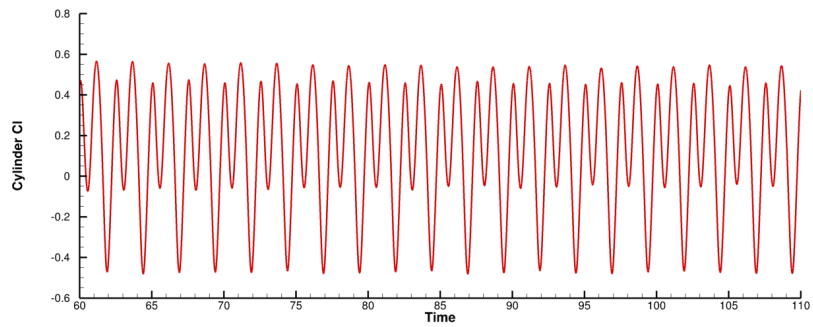
(d) h=0.0

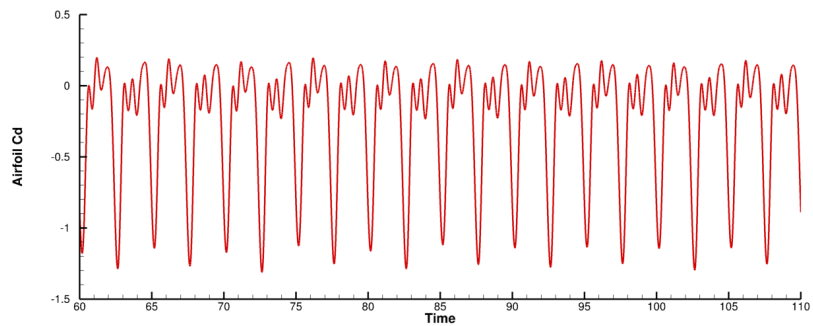Figure 11: Vorticity contours in one stroke period for case s=3.76 with double frequency
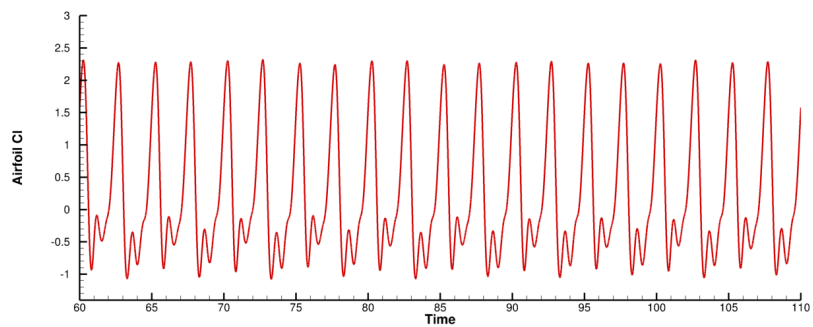
9

(a) Cylinder Cd

(b) Cylinder Cl

Figure 12: Cylinder drag and lift coefficients for case s=3.76 with double frequency

(a) Airfoil Cd

(b) Airfoil Cl

Figure 13: Airfoil drag and lift coefficients for case s=3.76 with double frequency

(a) Cylinder average force coefficients   (b) Airfoil average force coefficients
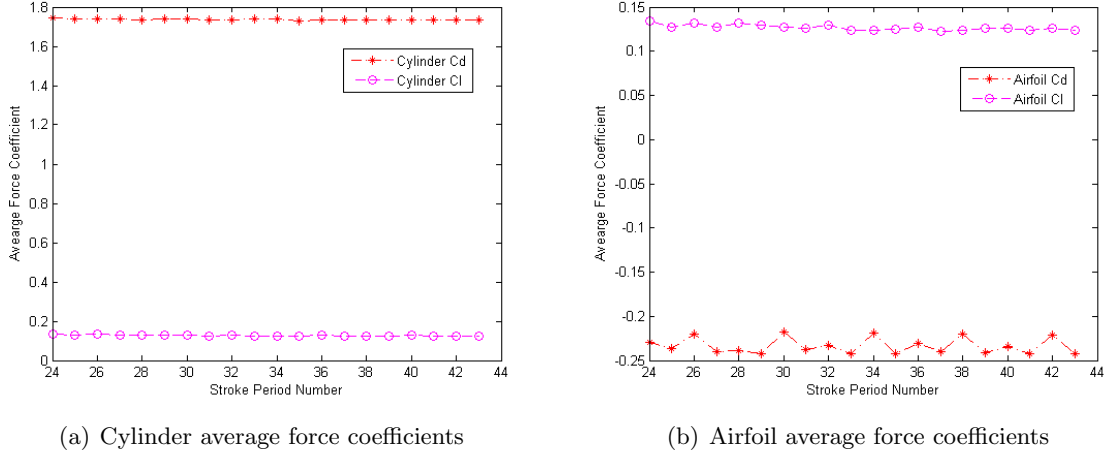
Figure 14: Average force coefficients for case s=3.76 with double frequency

5   Spectrum Analysis with the Fast Fourier Transform(FFT)

The Fast Fourier Transform(FFT) is a faster version of the Discrete Fourier Transform(DFT) which takes a discrete signal in the time domain and transforms that signal into its discrete frequency domain representation. It is very useful for analysis of time-dependent phenomena. In these two cases, FFT(implemented with Matlab) is employed to assess the frequency distribution of the drag and lift coefficients. The original drag and lift coefficients could be recovered by spectrum analysis method.

5.1   Case s=3.76

The cylinder drag and lift coefficients frequency distribution is shown in Fig. 15. Due to the symmetry of FFT, only the frequencies equal to or bigger than zero are examined.

For cylinder Cd, three dominant frequencies are 0Hz, 0.23Hz and 0.63Hz as shown in Fig. 15 (a). The corresponding amplitudes are 1.40, 0.23 and 0.19 respectively. So the original cylinder Cd could be roughly expressed as $Cd = 1.40 + 0.23\cos(2\pi \cdot 0.23t - 1.65) + 0.19\cos(2\pi \cdot 0.49t + 1.26)$ where t is time. This is consistent with the average cylinder Cd which oscillates near 1.40 as shown in Fig 6 (a). For cylinder Cl, two dominant frequencies are 0.20Hz and 0.43Hz as shown in Fig. 15 (b). The corresponding amplitudes are 0.41 and 1.08 respectively. The original cylinder Cl could be roughly expressed as $Cl = 0.41\cos(2\pi \cdot 0.20t + 0.54) + 0.43\cos(2\pi \cdot 0.43t + 1.78)$ where t is time.

The airfoil drag and lift coefficients frequency distribution is shown in Fig. 16. For airfoil Cd, three dominant frequencies are 0.23Hz, 0.40Hz and 0.63Hz as shown in Fig. 16 (b). The corresponding amplitudes are 0.24, 0.17 and 0.26 respectively. The original airfoil Cd could be roughly expressed as $Cd = 0.24\cos(2\pi \cdot 0.23t - 1.92) + 0.17\cos(2\pi \cdot 0.40t + 1.00) + 0.26\cos(2\pi \cdot 0.63t + 2.76)$ where t is time. For airfoil Cl, two dominant frequencies are 0.20Hz and 0.43Hz. The corresponding amplitudes are 0.95 and 0.94. The original airfoil Cl could be roughly expressed as $Cl = 0.95\cos(2\pi \cdot 0.20t + 0.39) + 0.94\cos(2\pi \cdot 0.43t + 0.50)$ where t is time.

The frequencies and corresponding amplitudes are summarized in Table 1.

5.2   Case s=3.5

The cylinder drag and lift coefficients frequency distribution is shown in Fig. 17. For cylinder Cd, three dominant frequencies are 0Hz, 0.23Hz, and 0.63Hz as shown in Fig. 17 (a). The corresponding amplitudes are 1.40, 0.23 and 0.19 respectively. So the original cylinder Cd could be roughly expressed as $Cd = 1.40 + 0.23\cos(2\pi \cdot 0.23t + 2.49) + 0.19\cos(2\pi \cdot 0.63t + 2.10)$.
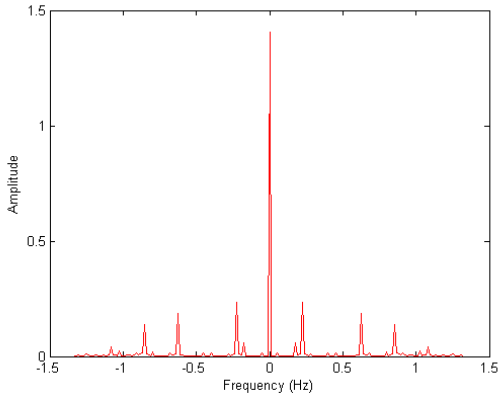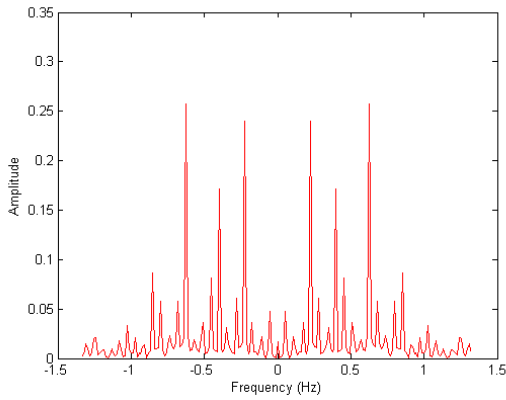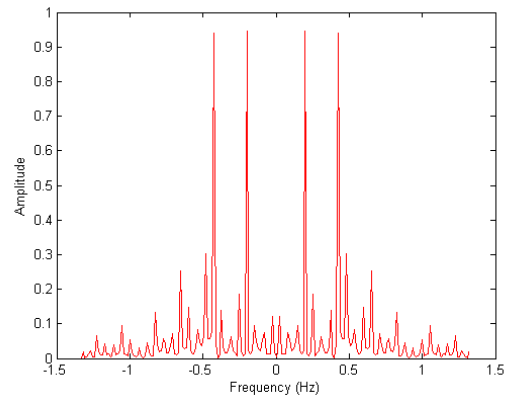
11

(a) Drag coefficient frequency distribution
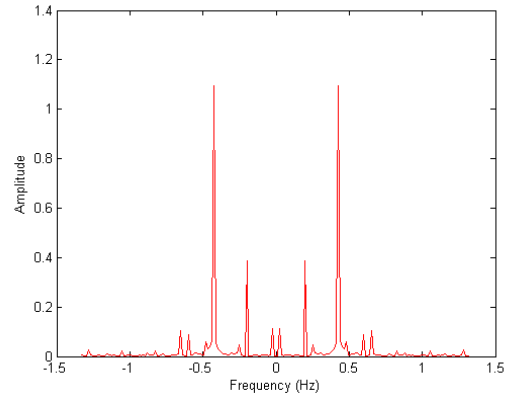
(b) Lift coefficient frequency distribution

Figure 15: Case s=3.76 cylinder drag and lift coefficient frequency distributions
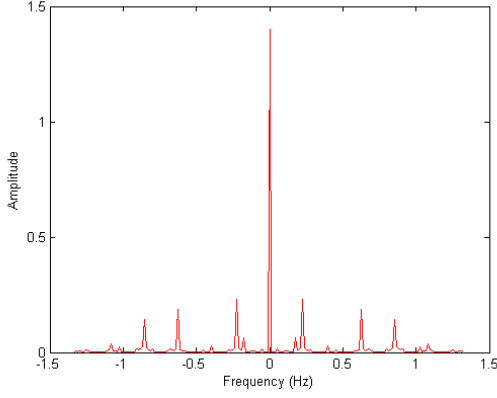

(a) Drag coefficient frequency distribution
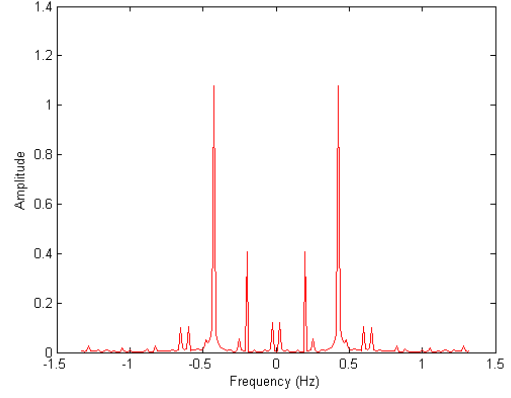
(b) Lift coefficient frequency distribution

Figure 16: Case s=3.76 airfoil drag and lift coefficient frequency distributions

Cylinder			Airfoil		
Object	Frequency	Amplitude	Object	Frequency	Amplitude
	0Hz	1.41		0.23Hz	0.24
Cd	0.23Hz	0.23	Cd	0.40Hz	0.17
	0.63Hz	0.19		0.63Hz	0.26
Cl	0.20Hz	0.41	Cl	0.20Hz	0.95
	0.43Hz	1.08		0.43Hz	0.94

Table 1: Case s=3.76 Spectrum Analysis

(a) Drag coefficient frequency distribution

(b) Lift coefficient frequency distribution

Figure 17: Case s=3.5 cylinder drag and lift coefficient frequency distributions
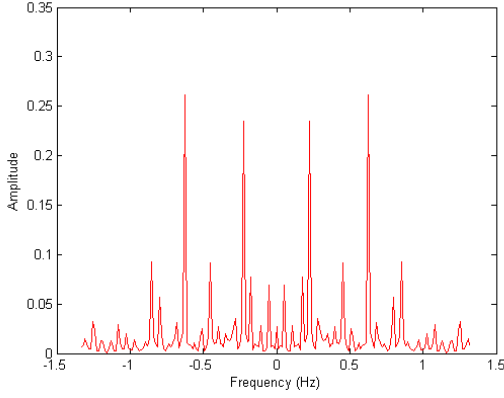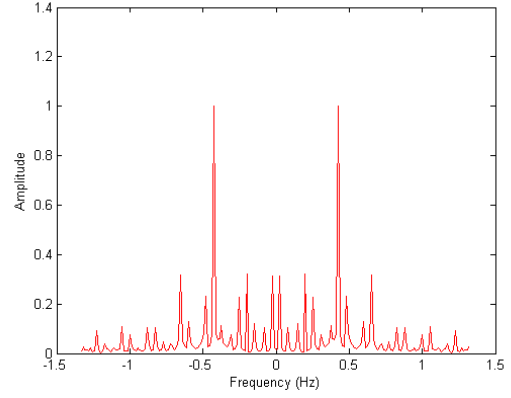

(a) Drag coefficient frequency distribution

(b) Lift coefficient frequency distribution

Figure 18: Case s=3.5 airfoil drag and lift coefficient frequency distributions

This is consistent with the average cylinder Cd which oscillates near 1.40 as shown in Fig. 10 (a). For cylinder Cl, two dominant frequencies are 0.20Hz and 0.43Hz as shown in Fig. 17 (b). The corresponding amplitudes are 0.41 and 1.08 respectively. The original cylinder Cl could be roughly expressed as $Cl = 0.41\cos(2\pi \cdot 0.20t + 0.54) + 1.08\cos(2\pi \cdot 0.43t - 1.37)$ where t is time.

The airfoil drag and lift coefficients frequency distribution are shown in Fig. 18. For airfoil Cd, there are two major frequencies which are 0.23Hz and 0.63Hz as shown in Fig. 18 (b). The corresponding amplitudes are 0.23 and 0.26 respectively. The original airfoil Cd could be roughly expressed as $Cd = 0.23\cos(2\pi \cdot 0.23t + 2.78) + 0.26\cos(2\pi \cdot 0.63t - 3.05)$ where t is time. For airfoil Cl, the dominant frequency is 0.43Hz. The corresponding amplitude is 1.00. The original airfoil Cl could be roughly expressed as $Cl = 1.00\cos(2\pi \cdot 0.43t + 0.52)$ where t is time.

The frequencies and amplitudes are summarized in Table. 2.

5.3   Conclusion

For cylinder Cl, there are two frequencies 0.20Hz and 0.43Hz, meaning vertex sheds at frequency 0.43Hz which is different from cylinder vibration frequency 0.20Hz. This happens because the cylinder vibration amplitude is relatively small.

In case $s = 3.76$, the airfoil Cl are dominated by the airfoil pitching frequency 0.20Hz and vertex shedding frequency 0.43Hz. However, in case $s = 3.5$, the airfoil Cl is only dominated by the vertex shedding frequency 0.43Hz due to the distance change.

13

Cylinder			Airfoil		
Object	Frequency	Amplitude	Object	Frequency	Amplitude
Cd	0Hz	1.40	Cd	0.23Hz	0.23
	0.23Hz	0.23		0.63Hz	0.26
	0.63Hz	0.19	Cl	0.43Hz	1.00
Cl	0.20Hz	0.41			
	0.43Hz	1.08			

Table 2: Case s=3.5 Spectrum Analysis

References

[1] C. Liang, K. Ou, S. Premasuthan, A. Jameson, and Z. J. Wang. High-order accurate simulations of unsteady flow past plunging and pitching airfoils. *Computers and Fluids*, 40:236–248, 2011.

[2] C. Liang, A. Jameson, and Z. J. Wang. Spectral difference method for two-dimensional compressible flow on unstructured grids with mixed elements. *Journal of Computational Physics*, 228:2847–2858, 2009.

[3] P. O. Persson, J. Peraire, and J. Bonet. Discontinuous Galerkin solution of the Navier-Stokes equations on deformable domains. *The 45th AIAA Aerospace Sciences Meeting and Exhibit*, AIAA paper 2007-513, 2007.

[4] K. Ou, C. Liang, and A. Jameson. High-order spectral difference method for the navier-stokes equations on unstructured moving deformable grids. *AIAA paper*, AIAA-2010-0541, 2010.

[5] M. L. Yu, Z. J. Wang, and H. Hu. A high-order spectral difference method for unstructured dynamic grids. *Computers and Fluids*, 48(1):84 – 97, 2011.

[6] K. Van den Abeele, C. Lacor, and Z. J. Wang. On the stability and accuracy of the spectral difference method. *J. of Scientific Computing*, 37:162–188, 2008.

[7] H.T. Huynh. A flux reconstruction approach to high-order schemes including discontinuous Galerkin methods. *AIAA Paper*, AIAA-2007-4079, 2007.

[8] R. J. Spiteri and S. J. Ruuth. A new class of optimal high-order strong-stability-preserving time discretization methods. *SIAM J. Numer. Anal.*, 40:469–491, 2002.